Deformation mechanisms of HCP- Multi Principal Element alloys (MPEAs) with equiaxed structures

S.J.Liang [a], T. Yoshino [a], R. Matusmoto [a], R. Sahara [b], Y. Toda [b], S. Matsunaga [a], Y. Yamabe-Mitarai [a*]

[a] Department of Advanced Materials Science, Graduate School of Frontier Sciences, The University of Tokyo, 5-1-5 Kashiwanoha, Kashiwa, Chiba 277-8561, Japan
[b] National Institute for Materials Science, 1-2-1 Sengen, Tsukuba, Ibaraki, 305-0047, Japan

[*]Corresponding authors' email: mitarai.yoko@edu.k.u-tokyo.ac.jp

Keywords: HCP-MPEAs, Thermomechanical processing, Equiaxed HCP phase, High temperature strength, Deformation mechanism

Abstract

The successful preparation of multi-principal element alloys (MPEAs) with stable single-phase FCC and BCC structures has allowed numerous studies to demonstrate that FCC and BCC-MPEAs not only possess excellent mechanical properties but also exhibit unique deformation mechanisms. In contrast, the solid solution strengthening and deformation mechanisms of HCP-MPEAs remain insufficiently understood due to the absence of alloys with stable single-phase HCP structures. In this study, single equiaxed HCP structures were successfully fabricated in $Ti_{45}Zr_{45}Al_{10}$, $Ti_{34}Zr_{33}Hf_{33}$, $Ti_{35}Zr_{30}Hf_{30}Al_5$, and $Ti_{30}Zr_{30}Hf_{30}Al_{10}$ alloys through the thermomechanical processing and subsequent heat treatment. The $Ti_{45}Zr_{45}Al_{10}$, $Ti_{30}Zr_{30}Hf_{30}Al_{10}$, and $Ti_{35}Zr_{30}Hf_{30}Al_5$ alloys exhibit excellent 0.2% proof strength from room temperature to 600 °C. The 0.2 % proof stress tends to increase with increasing mixing entropy (ΔS_{mix}) and the average atomic radius misfit (δ), consistent with calculations showing that the solid solution strengthening effect increases with increasing the δ. Density functional theory (DFT) calculations further indicate that Al contributes significantly to this increase in solid solution strengthening. The deformation is dominated by $(10\bar{1}0)$ prismatic slip. The low activation volume and high-stress exponent of these alloys at 600 °C suggest minor obstacles such as cluster or short-range order inhibit the movement of dislocation and lead to significant solid-solution strengthening.

1. Introduction

Multi-Principal Element Alloys (MPEAs) represent a new class of materials characterized by the presence of multiple principal elements, setting them apart from traditional alloys that typically contain only one or two principal elements [1]. Depending on the number of principal elements and their mixing entropy, MPEAs are often classified as high-entropy alloys (HEAs) or medium-entropy alloys (MEAs). In this study, we use the term MPEAs due to its broader definition, which accurately encompasses the diverse elemental composition of the alloys under investigation.

MPEAs are gaining significant interest due to their superior mechanical properties such as higher strength and ductility than conventional alloys [2–4]. Therefore, MPEAs are expected to be used in aerospace engine materials, such as FCC Ni-base-MPEAs for gas turbines [5–7] and BCC + HCP-MPEAs for compressors, to enhance some performance limitations found in traditional alloys. Moreover, in many FCC and BCC MPEAs, deforming and strengthening mechanisms different from those found in conventional alloys have been observed [4]. For example, in FCC-MPEAs, dislocation slip on the {111} plane is the primary deformation mechanism as in conventional FCC alloys, but many reports show that the minimum Critical Resolved Shear Stress (CRSS) value for dislocation movement is much higher in MPEAs than in conventional FCC alloys, which may enhance the strength [8]. It is also observed that the short-range order due to the irregular atomic arrangement results in a more significant hindrance to dislocation movement, which in turn leads to exhibiting more excellent mechanical properties than conventional alloys [9,10]. Similarly, in the BCC-MPEAs, it is also observed that cross slip is more likely to occur and will have a more substantial solid-solution strengthening effect in contrast to the conventional alloys [11,12].

Meanwhile, the HCP structure with excellent high-temperature properties is the main phase of high-temperature (HT)-Ti alloys. Solid-solution strengthening of the HCP phase in MPEA is also expected to enhance the heat resistance of HT-Ti alloys. Therefore, understanding the solid-solution strengthening and deformation mechanisms of HCP-MPEAs is necessary. Currently, single-phase HCP-MPEAs are categorized into three types, Type 1. rare-earth elements [13-21], Type 2. transition and platinum group elements [22-29], and Type 3. group 4 elements such as Ti, Zr, and Hf and rare-earth elements [30–48].

In Type 1 alloys, it has been reported that the compression strength of as-cast GdHoLaTbY was 108 MPa at room temperature [15]. The microstructure consisted of grains with a diameter of approximately 10 μm, along with segregated areas around grain boundaries. The low compressive strength at room temperature is attributed to the weak

interatomic interaction, primarily due to limited electronic charge transfer and elastic strain. Compressive strengths at room temperature for the as-cast DyErGdHoLuScTbY, DyGdHoLaTbY, and ErGdHoLaTbY were found to be 245, 205, and 360 MPa, respectively [16]. Among these, only ErGdHoLaTbY exhibited a single HCP phase, although a dendritic structure was clearly visible. In contrast, the other two alloys exhibited a two-phase structure consisting of HCP and FCC phases. In the case of as-cast YGdTbDyHo, an HCP structure with needle-like Y-rich precipitates was formed at the grain boundaries [17]. Micropillar compression tests were used to prove the mechanical properties within individual grains, revealing that plastic deformation occurs via the basal $< a > slip\ system,$ and strength was controlled by oxide particles. The tensile and compressive strengths of as-cast ScYLaGdTbDyHoErLu, which contains a single HCP phase with oxides oat grain boundaries, were also investigated [18]. Detailed microstructure analysis revealed the formation of Sc-rich nanoscale precipitates and twin structures within the grains. The tensile and compressive yielding strengths were measured at 213 and 251 MPa, respectively. It was suggested that non-basal slips dominate due to the smaller c/a ratio of 1.57, compared to the ideal value of 1.633. Deformation twins were induced during tensile deformation to relieve stress resulting from a limited-slip system. The creep behavior of as-cast GdHoLaTbY, which exhibits an equiaxed HCP phase, was studied at room temperature using nanoindentation [19]. The observed stress exponent ranged from 60 to 110, significantly higher than those of conventional alloys (~10). This result suggests that the synergistic diffusion between the component atoms, combined with severe lattice distortion in MPEAs, increases resistance to creep deformation.

In Type 2 alloys, the HCP structure in MPEAs has been predicted using CALPHAD modeling and *ab initio* molecular dynamics simulation [22]. Six CoReRu-based alloys were identified as HCP-MPEAs. Alloys with higher concentrations of platinum-group metals, such as IrMoRhRuW, were also found to exhibit an HCP structure based on thermodynamic calculations and the concept of Valence Electron Concentration (VEC) [23, 24]. In IrMoRhRuW, the crystal structure transitions from BCC to HCP and then FCC with increasing Ir and Rh contents. The HCP phase was stable within a temperature range of 1400-2200 ˚C. The mechanical properties of these alloys were evaluated at both room temperature and 1500 ˚C [25]. Despite the persistence of a dendritic structure following homogenization treatment at 1800˚C, the mechanical behavior of the HCP-MPEAs at elevated temperature was first investigated in [25]. The stress exponent was exceptionally high, measured at 15 and 8 at room temperature and 1500˚C, respectively, while a low activation volume was also observed. These results indicate that the formation

of chemical short-range order effectively impedes dislocation motion.

For catalytic applications, the HCP structure was obtained in IrOsReRhRu through thermal decomposition of single-source precursors [26] as well as in atomic-mixing RuRhPdPtIr catalyst [27]. Research has also explored the super conducting properties of HCP-HEAs [28, 29]. In RuOsMoWZr, the superconducting transition temperature was 2.9 K, with the upper critical field exceeding the Pauli limit, suggesting the possibility of unconventionally [28]. Structure investigations on $Mo_{35}W_xRe_yRu_zPd_5$ revealed a phase transition from HCP to σ-type and ultimately to BCC as the W content increased [29]. In HCP-$Mo_{35}W_{10}Re_{20}Ru_{30}Pd_5$, the superconducting transition temperature was 8.32 K.

As described above, investigations into the deformation mechanisms of Type 1 and Type2 alloys remain limited. Recently, research interest has shifted towards Type 3, Ti-containing HCP-MPEAs, including TiZrHf [30-35], TiZrSc [32, 39], TiZrHfSc [30, 32, 36-38], TiZrScNb [39], TiZrHfY [30], TiZrHfAl [33], TiZrHfAlSc [33, 35, 40-44], TiZrHfScRe [44], TiZrHfScRe [45], TiZrHfLaY [46], TiZrHfScYLa [47] and TiZrHfAlScNb [48]. Among these, a single HCP structure was achieved only in TiZrHf and TiZrSc. In other alloys, complex microstructures were observed, including dual HCP structures (e.g., TiZrHfSc, TiZrHfScY, TiZrHfLaY, TiZrHfScYLa,), partially ordered HCP structures ($D0_{19}$ structure in TiZrHfAlSc), HCP + second phase such as Zr_2Al in TiZrHfAl and HCP + BCC dual-phase structures with ω phase, depending on composition (e.g., TiZrScNb, TiZrHfScRe, TiZrHfAlScNb). These findings highlight the challenge of achieving a single HCP phase in these alloys.

Moreover, the HCP phase microstructure typically exhibits a martensite structure formed upon cooling from the stable BCC phase at high temperatures. Controlling the martensitic transformation remains challenging. Mechanical properties of these alloys have primarily been evaluated at room temperature through compression and tensile tests on as-cast samples featuring the martensitic structure [31, 36, 37, 39, 44, 48]. The yielding strengths of as-cast martensitic TiZrHf were reported as 773 MPa [30] and 901 MPa [31]. After solution treatment at 1000 ˚C in the BCC phase region followed by water quenching, the yielding strength increased to 967 MPa [32]. Upon annealing, the martensitic structure transformed into a plate-like HCP phase through diffusion.

Comparison between as-cast and heat-treated samples revealed notable differences. For instance, the yielding strengths of as-cast and heat-treated TiZrHfSc were 698 and 620 MPa, respectively [36]. While heat treatment reduced strength, the formation of cubic precipitates preserved similar strength levels. In TiZrHfScNb with HCP and BCC dual phases, the yielding strengths of as-cast and heat-treated samples were 1020 and 670 MPa, respectively [39]. The significant strength reduction after heat treatment was attributed to

microstructural coarsening.

The effect of alloy composition on the compressive strength has also been investigated [30]. In the as-cast condition, TiZrHf formed the equiaxed HCP structure, while TiZrHfSc exhibited dual HCP structures with a plate-like HCP phase. TiZrHfY and TiZrHfScY showed dendrite structures, with martensitic features observed in TiZrHfScY. Their compressive strengths were 773, 1001, 554, and 793 MPa, respectively. These results indicate that Sc addition enhances strength by promoting martensitic transformation, whereas Y addition decreases strength due to Y segregation in the interdendritic regions. The influence of microstructure on mechanical strength is significant, complicating the understanding of solid-solutioin strengthening in MPEAs.

Density functional theory (DFT) calculations for TiZrHfAlSc [41] revealed that Al addition decreases stacking fault energy, facilitating dislocation decomposition and hindering cross-slip. Additionally, Al strengthened covalent bonding and atomic interactions, thereby enhancing alloy strength. However, these effects are difficult to isolate in the presence of martensitic structures. Therefore, the fabrication of equiaxed HCP phases is critical for further investigations.

The fabrication of equiaxed HCP phase in Ti-containing HCP-MPEAs was explored to isolate and evaluate the solid-solution strengthening effects by minimizing the influence of martensitic structures. In our previous study, the formation of an equiaxed HCP structure in TiZrHfAl HCP-MPEAs was achieved through thermomechanical processing and heat treatment protocols typically applied to conventional Ti alloys [33]. However, the simultaneous formation of Zr_2Al also observed.

Kuang et al., [34] reported the successful development of an equiaxed HCP structure in TiZrHf HCP-MPEAs using rolling and heat treatment processes. Their finding indicated enhanced activation of <c+a> slip system and first-order pyramidal <a> dislocations, attributed to the high alloying concentration and localized compositional fluctuation. Despite these advancements, the deformation mechanism of the equiaxed single HCP phase in Ti-containing HCP-MPEAs remains insufficiently studied, highlighting the need for future investigation.

In this study, we aimed to achieve a single equiaxed HCP phase without second-phase precipitation in Ti-containing MPEAs to investigate the solid-solution strengthening effect. Through alloy composition design, thermomechanical processing, and subsequent heat treatment, we successfully formed a single equiaxed HCP phase in the TiZrAl, TiZrHf, and TiZrHfAl HCP-MPEAs. The objective of this research is to elucidate the deformation mechanisms and solid solution strengthening effects in TiZrAl, TiZrHf, and TiZrHfAl with TiZrHf with single equiaxed HCP structures. This study is expected to

address existing gaps in the understanding of HCP-MPEAs and contribute to the development of these advanced materials.

2. Materials and methods

2.1 Alloy composition design

In our previous study [33], the formation of an equiaxed HCP phase was applied for TiZrHf, TiZrHfAl, and TiZrHfAlSc by thermomechanical processing. However, the martensitic transformation occurred in TiZrHf and TiZrHfAlSc. The equiaxed HCP phase was successfully formed in only $Ti_{29}Zr_{23}Hf_{27}Al_{21}$ alloy. However, there was also the precipitation of the Zr_2Al phase, which may be attributed to the excessive addition of Al according to phase diagrams shown in Fig. 1 (a).

To address this issue, the composition of the $Ti_{29}Zr_{23}Hf_{27}Al_{21}$ alloy was further adjusted in the present study by gradually reducing the Al content, resulting in the design of $Ti_{30}Zr_{30}Hf_{30}Al_{10}$ ($TiZrHfAl_{10}$) and $Ti_{35}Zr_{30}Hf_{30}Al_5$ ($TiZrHfAl_5$) alloys. The equiatomic TiZrHf alloy was also selected to retry the formation of the equiaxed structure. Additionally, although Hf significantly stabilizes the HCP phase, its higher density and poor oxidation resistance limit its practical applications. Consequently, Hf was excluded, and TiZrAl was designed. To prevent the formation of intermetallic compounds like Ti_3Al due to excessive Al, the maximum Al addition was limited to 10 at%, based on the Ti-Al phase diagram shown in Fig. 1 (b). Ti and Zr were added in equal ratios to form a TiZrAl ternary alloy.

The specific compositions and corresponding parameters, such as mixing entropy ΔS_{mix} and average atomic radius misfit δ, of these alloys are summarized in Table 1.

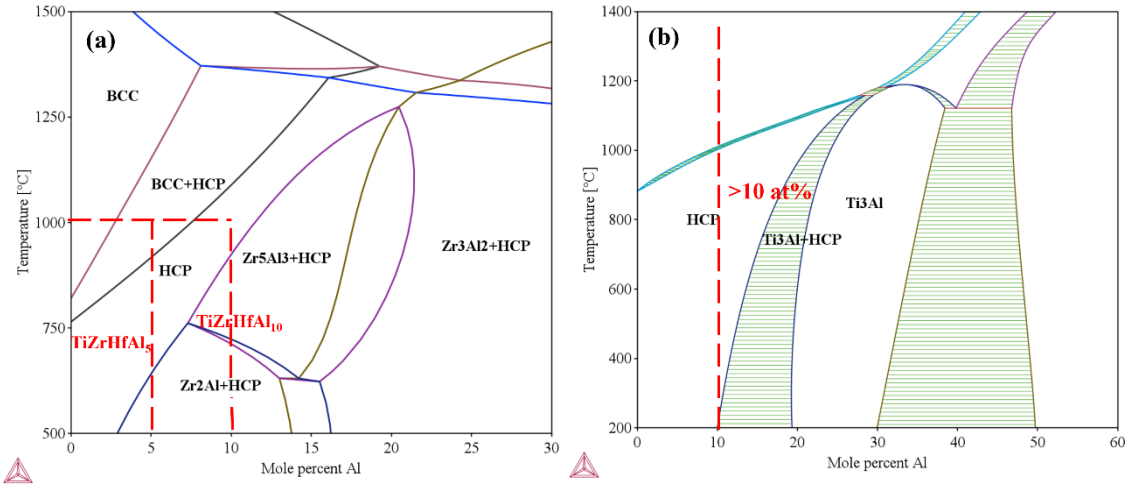

Fig.1 Phase diagram of (a) composition-dependent trend of $Ti_{50-x}Zr_{25}Hf_{25}Al_x$ as a function of Al content, and (b) Ti-Al binary, calculated using Thermo-Calc© software with the TCTI3 database.

Table 1 Nominal alloy composition, ΔS_{mix} and δ of the tested alloys

Alloy	**Composition (Atom ratio) (%)**				**ΔS (R)**	**δ (%)**
	Ti	Zr	Hf	Al		
TiZrHf	34	33	33	0	1.1	4.0
$TiZrHfAl_{10}$	30	30	30	10	1.3	4.4
$TiZrHfAl_5$	35	30	30	5	1.2	4.3
TiZrAl	45	45	0	10	1.0	4.8

The mixing entropy of MPEAs, ΔS_{mix}, is defined by the following equation (1):

$$\Delta S_{mix} = -R \sum_{i=1}^{n} x_i \ln x_i \quad (1)$$

where R is the gas constant (8.314 J/(K·mol)) and x_i is the atomic ratio of the *i-th* element.

The average atomic radius misfit δ is defined by the following equation (2):

$$\delta = 100\sqrt{\sum_i x_i \bullet \left(1 - \frac{r_i}{\bar{r}}\right)^2} \quad (2)$$

where the r_i is the atomic radius of *ith* element, and the $\overline{r}$ is the average atomic radius.

2.2 Alloy preparation and thermomechanical process

Raw materials of Ti (purity of 99.9%, Furuuchi Chemical), Zr (purity of 99.9%, Furuuchi Chemical), Hf (purity of 99.7%, Furuuchi Chemical), Al (purity of 99.99%, Furuuchi Chemical), were weighed in the appropriate amounts to attain the nominal composition as shown in Table 1. The 20 g ingots of the TiZrHf, $TiZrHfAl_5$, and $TiZrHfAl_{10}$ with the nominal composition, were prepared in an arc-melting furnace (NISSIN GIKEN Co., LTD) with a water-cooled copper plate under a protective argon atmosphere. The ingots were re-melted 5 times to ensure they were fully homogenized. Each drop shape ingot was 8 mm in height and 20 mm in diameter. In thermomechanical processing, the 20 g ingots were heated to 1000 ℃ for 5 minutes in an air furnace and subsequently hot-rolled. Each rolling step involved a reduction ratio of 10%, and after

each rolling step, the sample was reheated at 1000 ℃ for 5 minutes. This process resulted in a total reduction in thickness of 65%.

The TiZrAl alloy was prepared into larger ingots of 700 g using a Cold Crucible Levitation Melting (CCLM) to produce large experimental samples suitable for various mechanical evaluations. After homogenization at 900 °C, they were forged at room temperature using a 300-ton forging machine. The specimens were then heated to 900 °C and held for 5 minutes, followed by rolling (Grooved Roll Rolling Mill) in three passes. The first pass was done with a 35 mm radius groove, and the subsequent passes were done with grooves of 30 mm and 25 mm radii, with 5 minutes in a 900°C furnace after each pass. After the three rolling passes, the specimens were heated to 550°C and held for 5 minutes, and then the final roll was performed with a 15 mm radius groove.

2.3 Heat treatment

The rolled samples were subsequently subjected to heat treatment within the thermal stability temperature range of the HCP phase, as calculated using Thermo-Calc© software, to achieve fully recrystallized microstructures. During the heat treatment process, a $3\times3\times3$ mm^3 sample was cut from the rolled specimen and enclosed in a quartz tube filled with Ar gas to prevent oxidation. The heat treatment was conducted at temperatures ranging from 700 to 900℃ for 24 or 168 hours in a laboratory electric high-temperature box furnace (Y-1218-P, Yamadadenki, Co.Ltd), followed by either furnace cooling or water quenching.

2.4 Microstructural characterization

The crystal structure of the specimens was identified using X-ray diffraction (XRD). XRD analysis was conducted with a Rigaku SmartLab machine equipped with CuKα-radiation ($\lambda = 0.154$ nm). Measurements were performed at room temperature over a 2θ range of 10–90°, with a scanning rate of 10°/min and a step size of 0.02°. Data analysis was carried out using the PDXL-2 software (Rigaku), and phase identification was achieved by referencing the ICDD PDF-4 international diffraction database.

The heat-treated samples for microstructural observation were embedded in conductive phenolic resin (S60PA-K10, IMT Corporation). These mounted specimens underwent meticulous polishing using an automated polishing machine (SP-200, Subtech, Inc.) with a sequence of Grit320, 400, 600, 800, and 1000 polishing papers, followed by 3 μm and 1 μm polycrystalline diamond with silica suspension, and concluded with a final polishing step using a 5:1 mixture of colloidal silica and hydrogen peroxide solution. During each step, the polishing machine operated at 150 rotations per minute, with a load

of 0.5 MPa applied. The microstructure and phase composition of the alloys were characterized using a field emission scanning electron microscopy (FE-SEM, JEOL JSM-7200F) equipped with energy-dispersive spectroscopy (EDS, JEOL, EX-74600U4L20) and electron backscatter diffraction (EBSD) detectors (Digiview5, METEK, USA). The SEM and EBSD analysis were performed at an accelerating voltage of 20 kV. EBSD data were processed using OIM software, with step sizes ranging from 1 μm to 2 μm, depending on the magnification and specific area under investigation. Misorientation angles were categorized as low-angle grain boundaries (LAGB, 2°–15°) and high-angle grain boundaries (HAGB, >15°). The indexing was based on a CIF file standard for HCP-Ti metal and HCP-TiZr alloys, with detailed parameters derived from the inorganic crystal structure database(ICSD).

To further investigate the formation of the ordered Ti_3Al phase, transmission electron microscopy (TEM) was conducted using a JEOL FEM-2100F microscope operated at an accelerating voltage of 200 kV. TEM samples were prepared using a focused ion beam (FIB) system (JEOL JIB-4000). Thin lamellae with dimensions of approximately 10 μm × 5 μm × 0.1 μm were extracted and thinned to achieve electron transparency.

2.5 Evaluation of mechanical properties and deformation mechanisms

The recrystallized samples were cut into compression test specimens with gauge dimensions of 3 mm × 3 mm × 5 mm using a fine cutter or electric discharge machine (EDM). Compression tests were conducted to evaluate the mechanical properties at room temperature, 200, 400, and 600 °C, with a constant strain rate of 3×10^{-4}/s. Different deformation mechanisms respond uniquely to changes in strain rate during the deformation process. Therefore, the strain rate jump compression tests were performed at 200 and 600 °C, employing strain rates of 3×10^{-5}/s, 3×10^{-4}/s, and 3×10^{-3}/s, respectively, to investigate the deformation mechanisms. All tests, including both standard compression and strain rate jump tests, were carried out using a high-temperature compression machine (Shimadzu AG-X).

For $TiZrHfAl_{10}$ and TiZrAl alloys, after achieving a true plastic strain of 0.02 (ε_p= 2%), slip trace analysis was conducted to identify the active slip systems. This analysis utilized field emission scanning electron microscopy (FE-SEM, JEOL JSM-7200F) equipped with electron backscatter diffraction (EBSD) detectors (Digiview5, METEK, USA), focusing on areas deformed under different strain rates. EBSD data acquisition was optimized with step sizes between 0.3 μm and 0.5 μm, depending on the feature size and magnification level. Misorientation maps and crystallographic orientation data were analyzed using OIM software to correlate the observed slip traces with activity slip

systems.

2.6 DFT simulation

First-principles calculations were performed to model the TiZrHfAl series alloys using the Quantum ESPRESSO software [49], a plane wave-based implementation of density functional theory (DFT). The projector-augmented wave (PAW) method [50] was employed to represent the interactions between electrons and ions. At the same time, the exchange-correlation was described using the Perdew–Burke–Ernzerhof (PBE) parametrization of the generalized gradient approximation (GGA) [51].

Initially, these alloys were represented as $2 \times 2 \times 2$ hexagonal close-packed (HCP) supercell, which includes 128-atom using the Special Quasirandom Structure (SQS) model [52,53]. The SQS model is designed to mimic the properties of a random alloy within a finite supercell, ensuring that the local atomic environment closely resembles that of an ideal random mixture. Adapted for each specific alloy chemical composition, the $TiZrHfAl_{10}$ is represented as $Ti_{39}Zr_{38}Hf_{38}Al_{13}$, and $TiZrHfAl_5$ is represented as $Ti_{45}Zr_{38}Hf_{38}Al_7$ in 128 atoms. Brillouin zone integrations were performed using a set of 2×2×2 *k*-points. The cut-off energy for the plane wave expansion was set at 30 Ry. Gaussian smearing was used for the energy calculation with a smearing width of 0.01 Ry. The total energy was minimized over the degrees of freedom of the electron density and the ionic positions and structural parameters. Convergence threshold for energy a was set to 10^{-5} Ry Ry/bohr, respectively. Variable Cell Relaxation (VC-Relax tag in QE) was used to optimize both atomic positions and cell parameters, identifying the most stable configurations in terms of atomic arrangement and lattice dimensions. All calculations were performed on a supercomputer at the Institute for Solid State Physics, University of Tokyo.

3. Results

3.1 Microstructure formation

Fig. 2 presents the backscattered electron image of the microstructure formed in each alloy after rolling and subsequent heat treatment within their respective HCP phase regions. It can be observed that TiZrHf, TiZrAl, and $TiZrHfAl_5$ alloys developed an equiaxed structure through recrystallization after treatment at 700°C followed by furnace cooling. Similarly, $TiZrHfAl_{10}$ alloy exhibited an equiaxed structure after treatment at 800°C followed by water quenching. The X-ray diffraction (XRD) patterns illustrated in Fig. 3, confirm the presence of the HCP phase of space group 194 with lattice constants

of a = 3.15 Å, c = 5.03 Å, and c/a = 1.60 for the TiZrHf alloy, a = 3.11 Å, c = 4.90 Å, and c/a = 1.58 for the TiZrAl alloy, and a = 3.11 Å, c = 4.93 Å, and c/a = 1.59 for both the $TiZrHfAl_5$ and $TiZrHfAl_{10}$ alloys. The equiaxed grain structures were further confirmed as single HCP phases, with the average grain size of 86 μm for TiZrHf, 30 μm for TiZrAl, 55 μm for $TiZrHfAl_5$, 42 μm for $TiZrHfAl_{10}$, as measured by EBSD. These results verify that the thermomechanical and heat treatment processes described above can successfully form the desired equiaxed microstructures in both these alloys. In addition, although no peaks from other phases were observed in the XRD pattern of the $TiZrHfAl_{10}$ alloy, some contrasts, like precipitates, were observed, as shown in Fig. 2 (d). It might be due to the intermetallic compound Ti_3Al, commonly formed in Ti alloys. To investigate this, the alloy was examined by TEM, and the results are shown in Fig. 4. Selected Area Electron Diffraction (SAED) patterns derived from multiple crystallographic orientations of the alloy are shown. No superlattice spots in different zoon axes indicated the crystal structure is disordered HCP, not ordered $D0_{19}$ structure of Ti_3Al. This strongly suggests the absence of Ti_3Al intermetallic compounds in the $TiZrHfAl_{10}$ alloy.

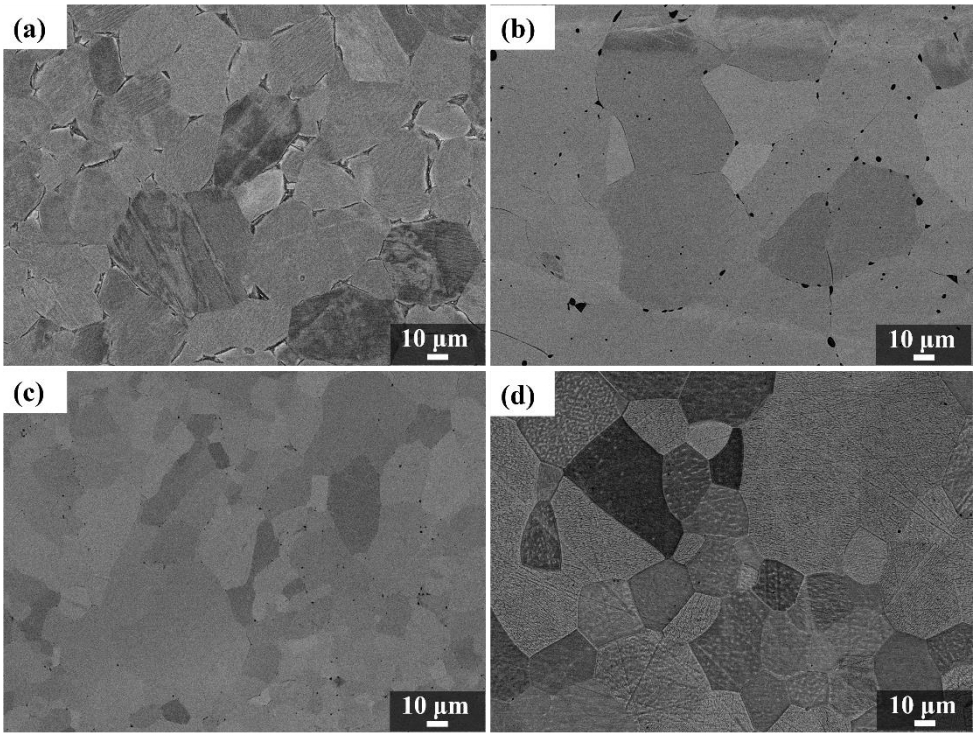

Fig. 2 Backscattered electron images of (a) TiZrAl, (b) TiZrHf, (c) $TiZrHfAl_5$ heat-treated at 700 °C, for 168h followed by furnace cooling, and (d) $TiZrHfAl_{10}$ at 800 °C, for 24h followed by water quench.

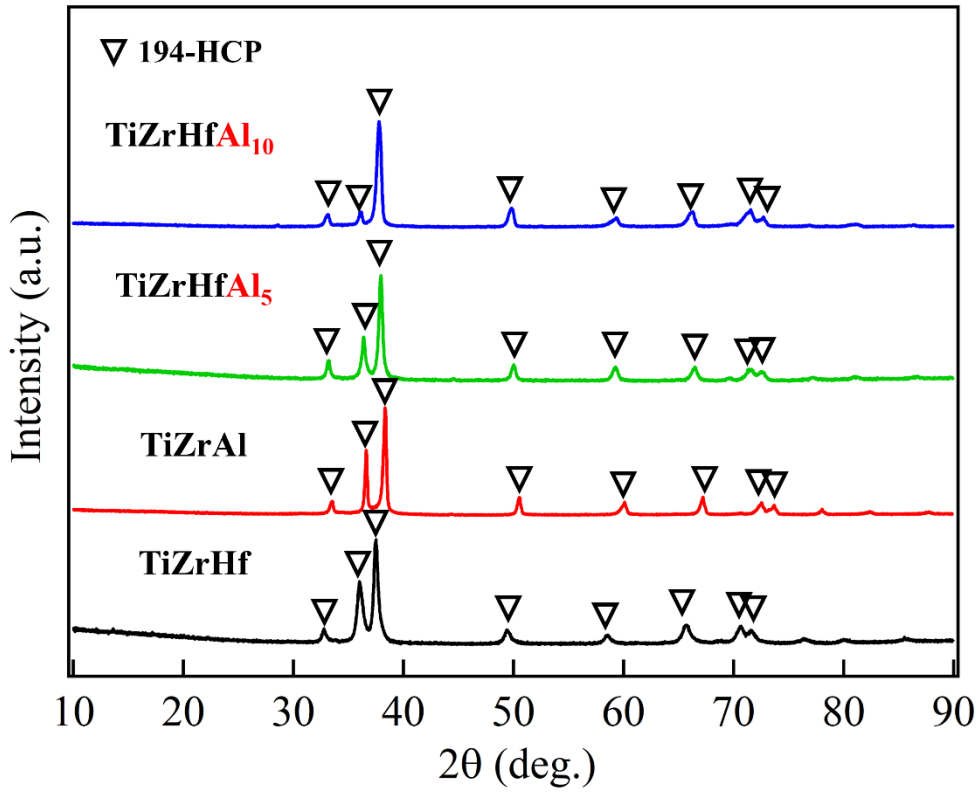

Fig. 3 X-ray diffraction (XRD) patterns of TiZrAl, TiZrHf, $TiZrHfAl_5$ heat-teated at 700 ℃, for 168h followed by furnace cooling, and $TiZrHfAl_{10}$ at 800 ℃, for 24h followed by water quench.

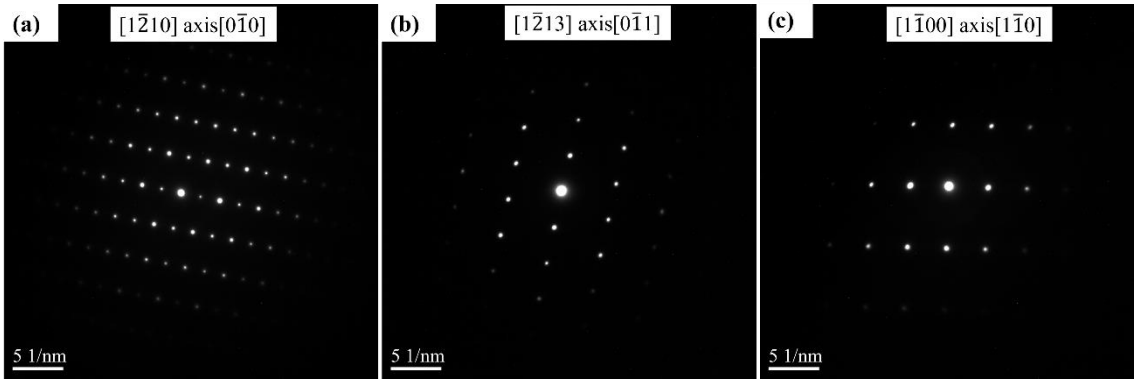

Fig. 4 Selected Area Electron Diffraction (SAED) patterns of $TiZrHfAl_{10}$ alloy in (a) [1$\bar{2}$10], (b) [1$\bar{2}$13] and (c) [1$\bar{1}$00] zone observed by TEM.

3.2 Mechanical properties

Fig. 5 illustrates the 0.2% proof strength of alloys with equiaxed HCP structures, measured by compression tests at room temperature, 200 ℃, 400 ℃, and 600 ℃. For comparison, the strengths of commercial high-temperature Ti alloys, such as Ti-6242,

TIMETAL834 [54] with bi-model structure and Ti-644 [55] with single equiaxed HCP structure are also plotted in Fig. 5. While bi-modal structures typically offer better strengthening in titanium alloys, HCP-MPEAs with single equiaxed structure studied here exhibit superior high-temperature strength compared to conventional high-temperature Ti alloys. Comparing the 0.2% proof stress of these HCP-MPEAs, the quaternary TiZrHfAl alloys exhibit significantly higher 0.2% proof stress than those of the ternaty TiZrHf and TiZrAl alloys. This can be attributed to the increase in mixing entropy (ΔS_{mix}), which enhances the effect of solid-solution strengthening. However, comparing the ternary alloys, TiZrAl alloy exhibits a notable increase in strength than TiZrHf, although the latter has a much higher mixing entropy (ΔS_{mix}), but the lower average atomic radius misfit (δ). This indicates that both ΔS_{mix} and δ have an essential influence on the solid solution strengthening effect. Additionally, the addition of Al can change the average atomic radius misfit (δ) to a greater extent, resulting in a more pronounced solid solution strengthening effect than that of Hf.

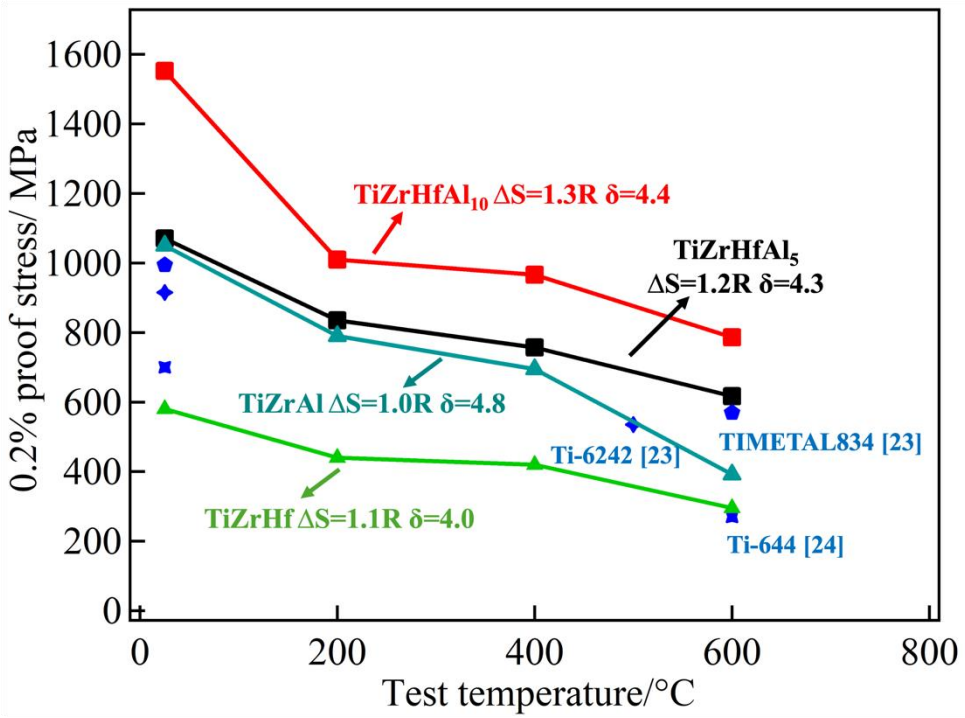

Fig. 5 0.2% proof stress depending on the test temperature of TiZrHf, TiZrAl, $TiZrHfAl_{10}$, and $TiZrHfAl_5$ with single equiaxed HCP phase obtained from the compression test, and comparison with other conventional high-temperature Ti alloys [23,24].

3.3 Deformation behavior of alloys by strain rate jump test

The compressive stress-strain curves obtained from the strain rate jump test at 200 and 600 ℃ for these alloys are depicted in Fig. 6. The change in strain rate causes a sharp

increase in stress. The 0.2% proof stress corresponding to each different strain rate at 200 and 600℃ was measured and summarized in Table 2, except for the change at 200 ℃ (Fig. 6 (c)) for TiZrAl, which was too small to be observed.

An Arrhenius-type equation (3) was used to express the strain rate $\dot{\varepsilon}$ [56].

$$\dot{\varepsilon} = A\sigma^n exp\left(-\frac{Q}{RT}\right) \quad (3)$$

where A is the material constant, σ is the stress, n is the stress exponent, Q is the activation energy for deformation, R is a gas constant, and T is the temperature. Taking the natural logarithm of both sides gives (4):

$$\ln \dot{\varepsilon} = \ln(A) + n\ln \sigma - \frac{Q}{R}\left(\frac{1}{T}\right) \quad (4)$$

The stress exponent n can be calculated from the slope using a double-log plot of $\ln \dot{\varepsilon}$ and $\ln \sigma$ in equation (4). The 0.2% proof stress was used as σ to estimate the stress exponent n.

Fig. 7 illustrates the double logarithm plot of the strain rate ($\dot{\varepsilon}$) versus 0.2% proof stress (σ) at 200 and 600 ℃ for each alloy. At 200 ℃, the stress exponents are significantly high, with values of 27 for the $TiZrHfAl_{10}$ alloy, 20 for the TiZrHf alloy, and 18 for the $TiZrHfAl_5$ alloy. At 600 °C, the stress exponents decrease compared to those at 200 °C, but the alloys still exhibit values range from 13 to 15, except for the TiZrAl alloy. TiZrAl has a relatively low mixing entropy and exhibits a stress exponent of 7, which is still higher than that of conventional Ti alloys, which typically range from 3 to 5 [57, 58].

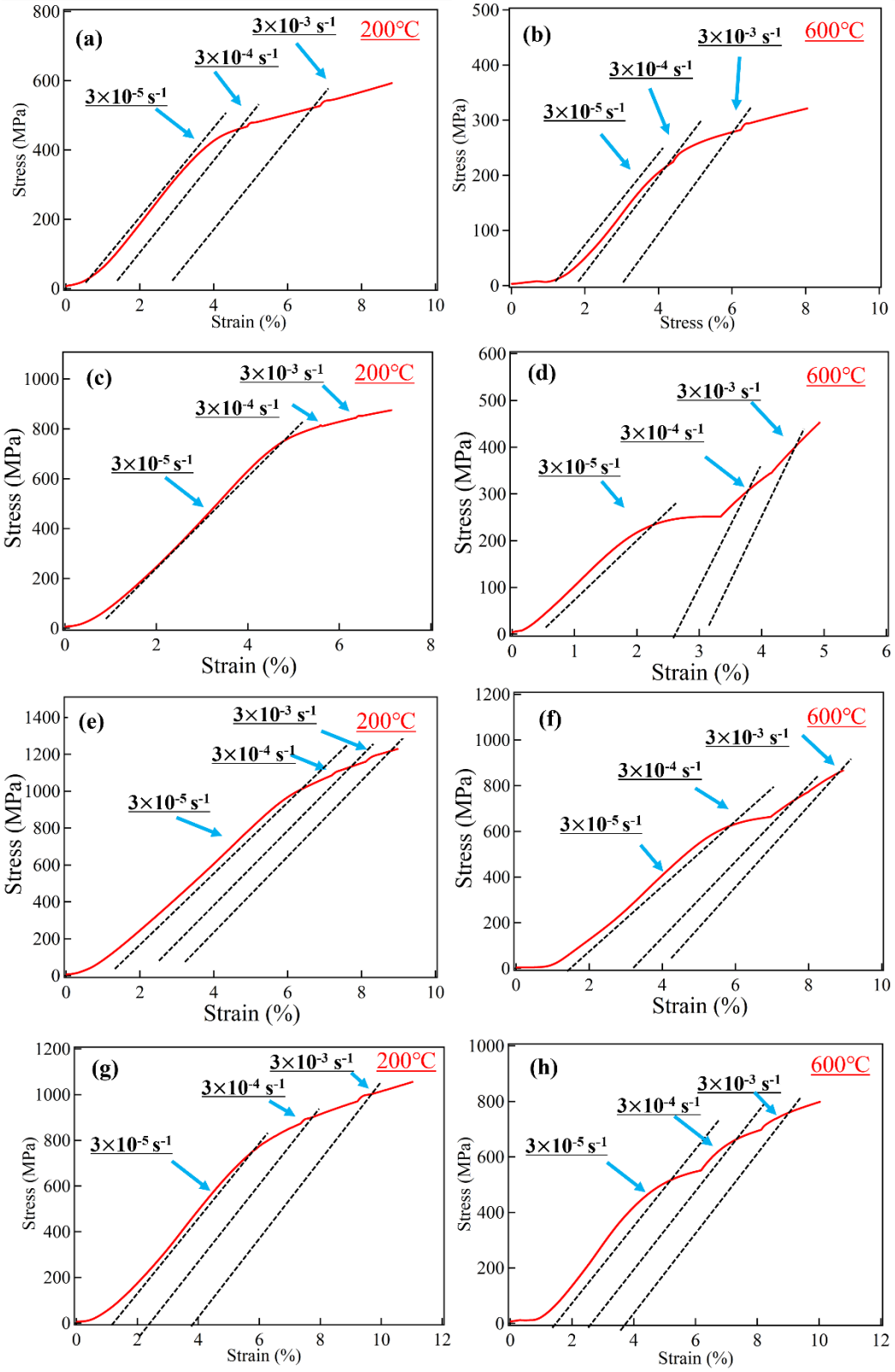

Fig. 6 Stress and strain curves at 200 and 600 °C by strain rate jump test for (a), (b): TiZrHf, (c), (d): TiZrAl, (e), (f): $TiZrHfAl_{10}$, (g), (h): $TiZrHfAl_5$ alloys.

Table 2 The 0.2% proof stress corresponds to each strain rate at 200 and 600℃.

Temperature (℃)	Alloy	0.2% proof stress (MPa)		
		3×10^{-5}/s	3×10^{-4}/s	3×10^{-3}/s
200	TiZrHf	435	482	546
	TiZrAl	-	-	-
	$TiZrHfAl_{10}$	1022	1126	1208
	$TiZrHfAl_5$	770	900	1000
600	TiZrHf	220	254	296
	TiZrAl	237	343	456
	$TiZrHfAl_{10}$	625	754	853
	$TiZrHfAl_5$	478	648	740

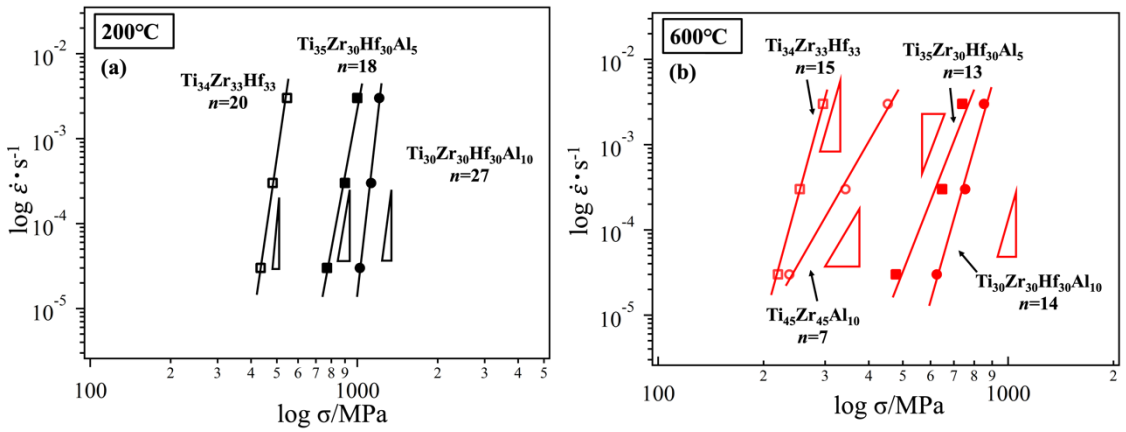

Fig. 7 Double logarithm plot of the stress and strain rate for TiZrHf, TiZrAl, $TiZrHfAl_5$, and $TiZrHfAl_{10}$ alloys obtained by strain rate jump test at (a) 200 and (b) 600℃.

The high-temperature deformation is a thermally activated process, and the mechanisms involved in compressive deformation can be quantitatively described using the activation volume ($V*$). This volume represents the space within which a dislocation can move by overcoming obstacles during deformation [59, 60]. Typically expressed in units of b^3 (where b is the Burgers vector), the activation volume ($V*$) is defined by the following equation (5).

$$V^* = \sqrt{3}kT(\partial ln\varepsilon/\partial\sigma) \qquad (5)$$

where k is the Boltzmann's constant, and the T is the absolute temperature. The activation

volumes at 200 and 600 ℃ were calculated and summarized in Table 3.

Table 3 The activation volumes at 200 and 600 ℃ for TiZrHf, TiZrAl, $TiZrHfAl_5$, and $TiZrHfAl_{10}$ alloys.

Alloy	**Temperature (℃)**	**3×10^{-5} - 3×10^{-4} (s^{-1})**	**3×10^{-4} - 3×10^{-3} (s^{-1})**
		V* (**b^3**)**	
TiZrHf	200	19.5	14.3
	600	49.8	40.3
TiZrAl	200	-	-
	600	15.9	15.4
$TiZrHfAl_5$	200	7.1	9.2
	600	10.0	18.4
$TiZrHfAl_{10}$	200	8.8	11.2
	600	12.8	17.1

At 200 °C, the activation volumes for the ternary alloy TiZrHf, which has relatively low mixing entropy, range from 10 to 20 b^3. In contrast, the activation volumes for the $TiZrHfAl_{10}$ and $TiZrHfAl_5$ alloys, which exhibit higher mixing entropy, are observed to be below 10 b^3. As the test temperature and strain rate increase, the activation volumes show a slight rise. However, at 600 °C, the activation volumes for most of the alloys remain below 20 b^3, except for the TiZrHf alloy, which displays a significant increase to 40–50 b^3. This suggests that, at 600 °C, the deformation mechanism in the TiZrHf alloy is primarily influenced by thermally activated mechanisms.

3.4 Slip behavior by slip trace analysis

According to the slip line morphology information and the crystallographic orientation data were collected by SEM and EBSD, the active slip modes during compression test can be determined by slip trace analysis. The specific analysis method as described in the other works [61, 62], begins by calculating the theoretical angles that various slip systems form with the direction of applied stress, based on EBSD and pole figures. The observed slip traces in the specimens are then compared to these angles. If a slip trace aligns or is parallel to one of these angles, it is concluded that the trace was produced by that slip system.

As shown in Fig. 8, grains with clearly visible slip lines in different orientations were analyzed in both TiZrAl and $TiZrHfAl_{10}$ alloys. The analysis revealed that all identified slip traces originated from the $(10\bar{1}0)$ prismatic slip, which is consistent with the

dominant slip system in conventional HCP-Ti alloys at room temperature [63].

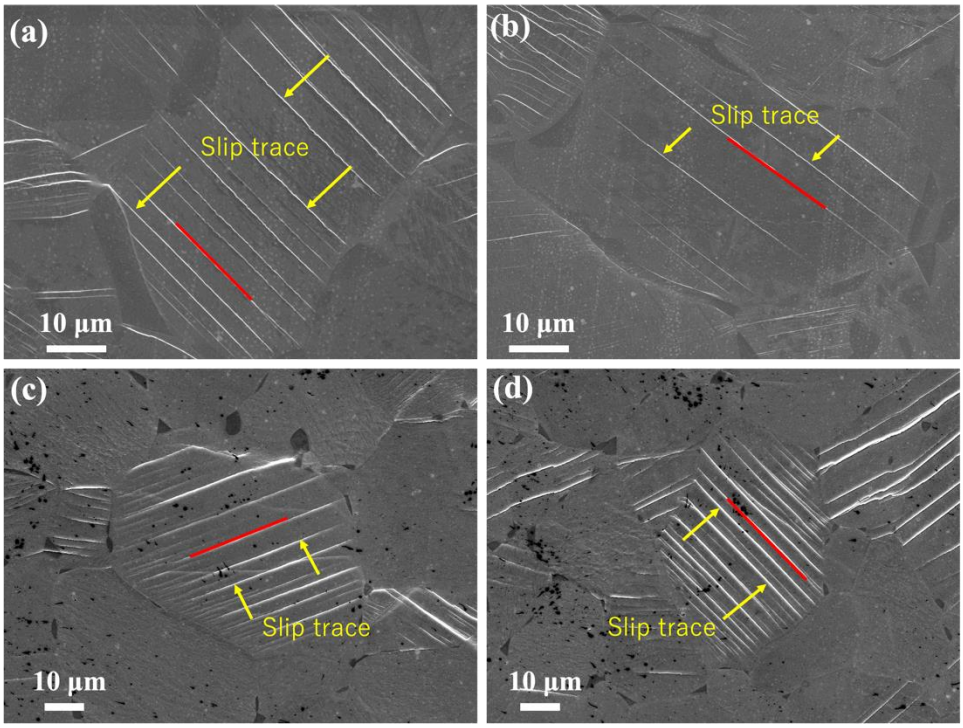

Fig. 8 Secondary electron images showing selected grains for slip trace analysis in (a), (b): TiZrAl alloy and (c), (d): $TiZrHfAl_{10}$ alloy

3.5 The electric charge density calculated by DFT

The electric charge density indicates the bonding of constituent atoms that affects solid solution strengthening. The electric charge density of $TiZrHfAl_5$ and $TiZrHfAl_{10}$ alloys, calculated on the slip plane of {0001} and $\{10\bar{1}0\}$ using the HCP-SQS model and VC-relaxed are depicted in Fig. 9. Fig. 9(a, c) show the electric charge density on the {0001} plane, while Fig. 9(b, d) display the electric charge density on the $\{10\bar{1}0\}$ plane. The regions marked by red arrows appear higher electron density between the atomic pairs. Observations from the {0001} plane highlight not only elevated electron densities for Ti-Zr and Ti-Hf pairs but also notable densities for Ti-Al pairs in $TiZrHfAl_5$ (Fig. 9 (a)), and Hf-Al pairs, Zr-Al pairs in $TiZrHfAl_{10}$ (Fig. 9 (c)). These observations indicate potential sites for enhanced solid-solution strengthening due to Al addition. The $\{10\bar{1}0\}$ plane similarly shows heightened electron densities for Ti-Zr, Ti-Hf, Ti-Al, and Zr-Al pairs, suggesting a uniform enhancement across various atomic interactions.

The electric charge density was simulated in TiZrHf [64] and it was found that the bonding between Ti-Hf was weaker than the bonding between other elements. The bonding length during the tensile test was also simulated and the bonding length between

Ti-Hf became longer than others during the test. It suggested that deformation mainly progressed due to the elongation of the bonding between Ti-Hf. In our calculation, the specific weak bonding was not observed. It is suggested that electric charge density became denser by Al addition and the bonding between two atoms became stronger in TiZrHfAl than in TiZrHf. This can be imagined from the strength of TiZrHfAl was higher than that of TiZrHf as shown in Fig. 5.

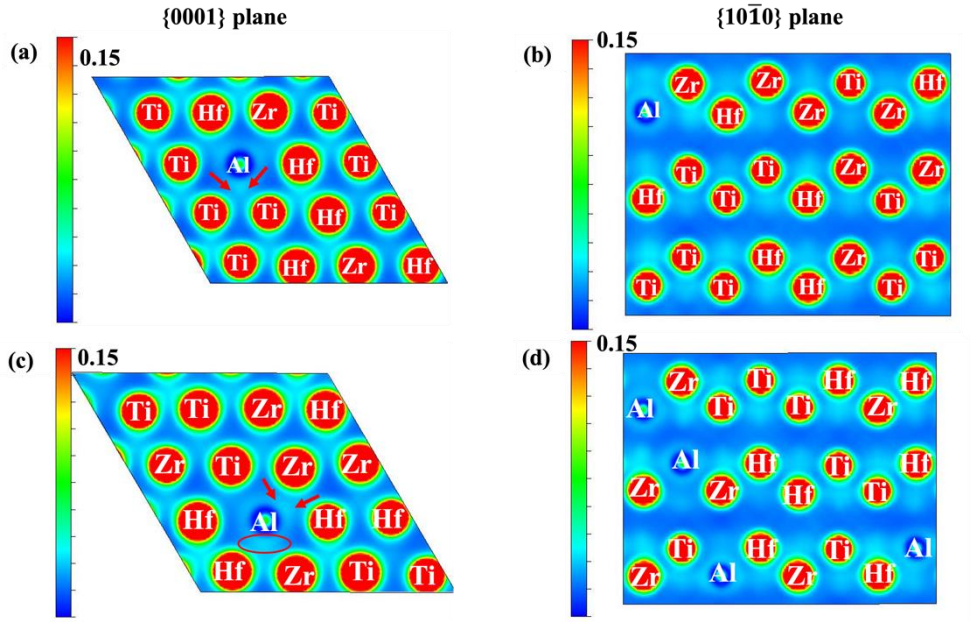

Fig. 9 Electric charge density of $TiZrHfAl_5$ (a, b), and $TiZrHfAl_{10}$ (c, d) alloys on the {0001} plane and the {10$\bar{1}$0} plane calculated by DFT.

4. Discussion

4.1 Discussion of deformation mechanisms by strain rate jump test

The thermal activation processes investigated through stress-strain rate jump tests at varying temperatures and strain rates help characterize the underlying deformation and strengthening mechanisms. As mentioned previously, the Ti-containing HCP-MPEAs in this study exhibited overall larger stress exponents (n). The activation volumes (V^*) of the HCP-MPEAs from this study and those from other referenced alloys are summarized and plotted in Fig. 10 for comparison.

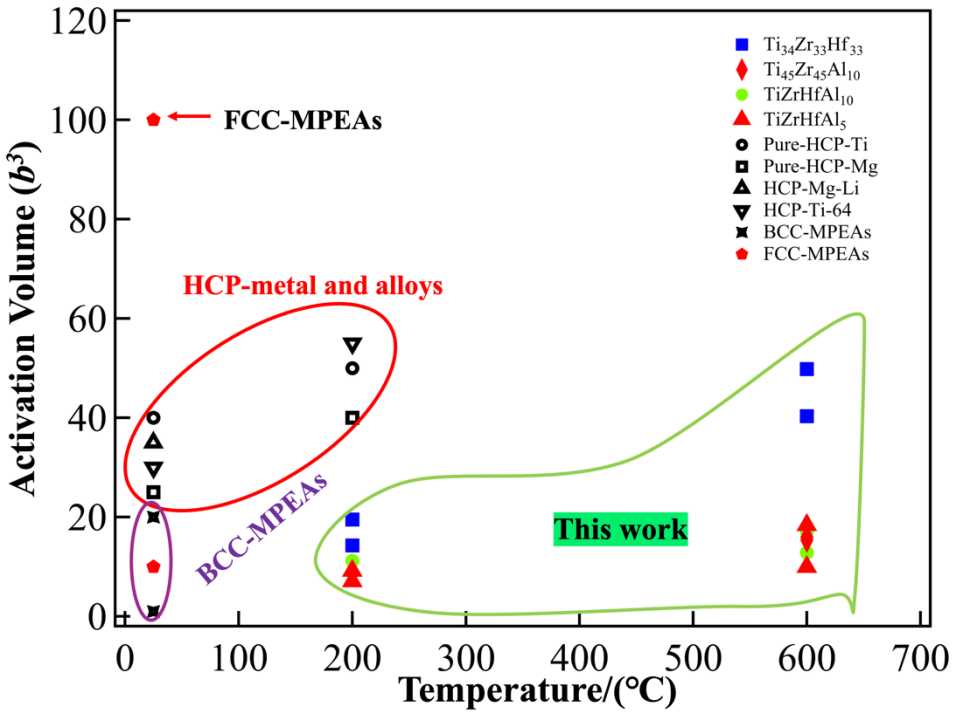

Fig. 10 The activation volumes of the HCP-MPEAs from this study and those from other referenced alloys [65–69].

According to Liu et al., [65], the measured activation volume of pure Ti metal with an HCP crystal structure at a deformation rate of 10^{-4} s^{-1} is approximately 35 b^3 at 250°C and remains around 50 b^3 in the temperature range of 350-450°C. Ti-6Al-4V (Ti64) alloys with an HCP structure exhibit an activation volume similar to that of pure Ti, approximately 35 b^3 at room temperature, rising to about 60 b^3 as the temperature increases to 200 °C [66]. Other HCP metals and alloys, such as pure Mg and Mg-Li alloys, also reported [67] that have activation volumes ranging from 25 to 35 b^3 at room temperature. In contrast, the activation volumes of the HCP-MPEAs in this study, both at 200°C and 600°C, are much lower than those of conventional HCP metals at room temperature.

When comparing the activation volumes to other MPEAs, it is difficult to directly compare them with other HCP-MPEAs due to the limited amount of activation volume data reported for HCP-MPEAs. However, according to Hong et al., [68] the activation volumes of FCC-MPEAs at room temperature are 10-100 b^3, whereas, in conventional FCC alloys, they range from 100 to 1000 b^3 in conventional FCC alloys. Xiao et al., [69] reported that most of the activation volumes for BCC-TiZrHfNb series MPEAs are concentrated in the range of 1-20 b^3. This suggests that, like FCC-MPEAs, HCP-MPEAs

also exhibit a smaller activation volume than conventional alloys.

The larger stress exponents (n) and smaller activation volumes (V^*) observed, compared to typical HCP alloys, suggest that deformation in these alloys is primarily dominated by dislocation glide, with only a minimal volume involved in atomic rearrangements or dislocation motion necessary for the deformation process. Consequently, it is postulated that the elevated stress exponent in the Ti-containing HCP-MPEAs could be attributed to dislocations navigating through small obstacles, such as atomic clusters or short-range order structures. These small obstacles act as atomic size precipitates, and they lead to high stress exponent and low activation volume. Atomic clusters and short-range order structures are explained in the next paragraph.

Regarding the strengthening mechanisms, the Labusch model [70] is traditionally used to explain the strengthening in dilute alloys. According to this model, dislocations must overcome the stress fields created by solute atoms to continue moving. Overcoming these stress fields requires additional stress, which increases the yield strength of the alloys. In the Labusch model, it is shown that a higher concentration of solute atoms leads to a more pronounced solid-solution strengthening effect. Wu et al.,[71] found experimentally that this model is still applicable in MPEAs with higher concentrations of solute atoms, and they introduced an improved Labusch model. The distribution of atoms in MPEAs is more random and complex than that observed in conventional dilute alloys. This complexity leads to the formation of localized atomic clusters and short-range ordered arrangements, which result in significant local fluctuations in the stress field, such as extra stress fields caused by element-element interaction, which have been reported by S. Yoshida et al. [72]. Consequently, the energy required for dislocations to traverse these irregular barriers also varies greatly. However, due to the density of these barriers being higher than in conventional alloys, the overall energy required for dislocation movement is typically higher, thereby enhancing the strengthening effect.

4.2 Discussion of deformation behaviors by slip trace analysis

Deformation in HCP alloys primarily occurs through <a> direction slip systems, which include basal, prismatic, and pyramidal slips [73]. Increasing the content of solid solution elements leads to a more significant distortion of the crystal lattice and alters the c/a ratio. This alteration can activate previously inactive slip systems in the <c> direction, facilitating both <a> and <c+a> cross slip. As a result, this activation enhances the alloy's ductility by allowing more diverse deformation mechanisms.

In pure Ti, Zr, and Hf, prismatic slip is typically the active slip system [63,74]. However, with the addition of Al, basal slip can also become active. Therefore, it was initially

expected that in the TiZrAl and $TiZrHfAl_{10}$ alloys, the addition of Al might activate basal slip. Contrary to these expectations, at 2% plastic deformation, the slip traces observed in both TiZrAl and $TiZrHfAl_{10}$ alloys were attributed to $(10\bar{1}0)$ prismatic slip. This indicates that, despite the potential for Al to activate basal slip, the deformation mechanisms in this alloy remain dominated by prismatic slip. This suggests that, although the addition of Hf and Al increases the entropy of mixing, it does not significantly alter the c/a ratio (1.575 and 1.585), leaving the deformation mechanism unchanged. Furthermore, Kuang et al., [34] reported that in the $Ti_{38}Zr_{31}Hf_{31}$ (c/a =1.586) and $Ti_{34}Zr_{33}Hf_{33}$ (c/a =1.584), at 8% plastic deformation, although prismatic <a> slip was still dominant, the rate of <c+a> slip increased compared to pure Ti (c/a =1.587), even their c/a did not change significantly. Therefore, as the plastic deformation increases, <c+a> pyramidal slip occurrences may become more prominent in TiZrAl and TiZrHfAl series alloys.

4.3 Discussion of solid solution strengthening (SSS) in HCP-MPEAs

Solid-solution strengthening (SSS) is widely known as the principal strengthening mechanism in MPEAs, as it is in conventional alloys. The high concentration of constituent elements in MPEAs gives rise to considerable SSS effects. However, the distinction between solute and solvent atoms in MPEAs presents a significant challenge, limiting the development of computational models for estimating the stress contributions from SSS. In the classical Labusch model, the SSS mechanism is generally described in terms of atoms randomly dispersed within a solvent. The interaction between solute atoms and dislocations is augmented by the misfit in their atomic radius (r) and shear modulus (G). Currently, the classical Labusch equation, expressed as (6), has been successfully modified and applied to calculate SSS in some MPEAs [70, 75].

$$\Delta\sigma = (\sum \Delta\sigma_i^{3/2})^{2/3} \quad (6)$$

Where $\Delta\sigma_i$ is the stress contributed of element i.

Qiao et al, reported that the $\Delta\sigma_i$ caused by element i can be expressed as (7) [76].

$$\Delta\sigma_i = ZGf_i^{4/3}c_i^{2/3} \quad (7)$$

where Z is a material-dependent dimensionless constant, which is typically on the order of 0.004 [77], G is the shear modulus of the concentration of metal, c_i is the concentration of element i, and f_i is the mismatch parameter. The f_i parameter can be calculated by equation (8)

$$f_i = \sqrt{\delta G_i^2 + \alpha^2 \delta r_i^2} \quad (8)$$

where δG_i is the atomic modulus mismatch parameter δr_i is the atomic size mismatch parameter, and α is a constant, which depends on the type of the mobile dislocations. Generally, α is 2–4 for the screw dislocations and ≥16 for the edge dislocations [78,79]. In this study, a value of 16 was chosen because the deformation behavior of HCP alloys is primarily influenced by edge dislocations.

The mismatch parameters δG_i and δr_i can be calculated using the method described in Refs. [80] and [81]. In the HCP lattice, each atom has 12 nearest-neighbor atoms, thus forming a 13-atom cluster. If the local concentration equals the average concentration of the alloy, the local environment around element *i* can be roughly estimated. Thus, element *i* will have $N_j = 13c_j$ of *j*-atom neighbors and $N_i = 13c_i - 1$ of *i*-atom neighbors ($j \neq i$). Consequently, the atomic size mismatch δr_i and atomic modulus mismatch δG_i in the vicinity of element *i* can be estimated as an average of the atomic size difference δr_{ij} and shear modulus difference δG_{ij} of this element with its neighbors, respectively, by

$$\delta r_i = \frac{13}{12}\sum c_j \delta r_{ij} \tag{9}$$

$$\delta G_i = \frac{13}{12}\sum c_j G_{ij} \tag{10}$$

where c_j is the atomic fraction of element *j* in the alloy.

$$\delta r_{ij} = 2(r_i - r_j)/(r_i + r_j) \tag{11}$$

$$\delta G_{ij} = 2(G_i - G_j)/(G_i + G_j) \tag{12}$$

The calculated SSS ($\Delta\sigma$) values of the HCP-MPEAs in this study, obtained using Eq. (6-12), are as follows: TiZrHf is 103.5 MPa, TiZrAl is 115.1 MPa, $TiZrHfAl_5$ is 106.3 MPa, and $TiZrHfAl_{10}$ is 106.1 MPa. As shown in Fig. 11(a), there is a correlation between the average atomic radius misfit (δ) values and the SSS ($\Delta\sigma$) values for Ti-containing HCP-MPEAs with a single HCP structure: larger value of δ results in higher $\Delta\sigma$. The increase in $\Delta\sigma$ is attributed to the greater lattice mismatch in the HCP-MPEAs.

The SSS ($\Delta\sigma$) effect of each constituent element was calculated by Eqs. (6-12) in the corresponding alloys. They are labeled in different colors and shown in Fig. 11 (b) in the same order as in Fig. 11(a). According to this, it can be observed that, due to the relatively small atomic radius misfit between Hf and Zr, the solid solution strengthening in TiZrHf alloys mainly arises from the interaction of Ti ($\Delta\sigma_{Ti}$), such as Ti-Zr and Ti-Hf bonds. When Al is further added to TiZrHf alloys, the larger radius misfit between Al and (Zr, Hf) enhances the solid-solution strengthening effect caused by Zr-Al and Hf-Al

interactions. However, despite the equal concentrations of Zr and Hf, $\Delta\sigma_{Zr}$ is greater than $\Delta\sigma_{Hf}$ in TiZrHfAl, indicating that Zr-Al interactions have a more substantial solid-solution effect than Hf-Al. The addition of Al reduces the strengthening effect of Ti, but there is not much difference in the total strengthening effect of Ti, Zr, and Hf in TiZrHf and TiZrHf Al because the contents of Al is small.

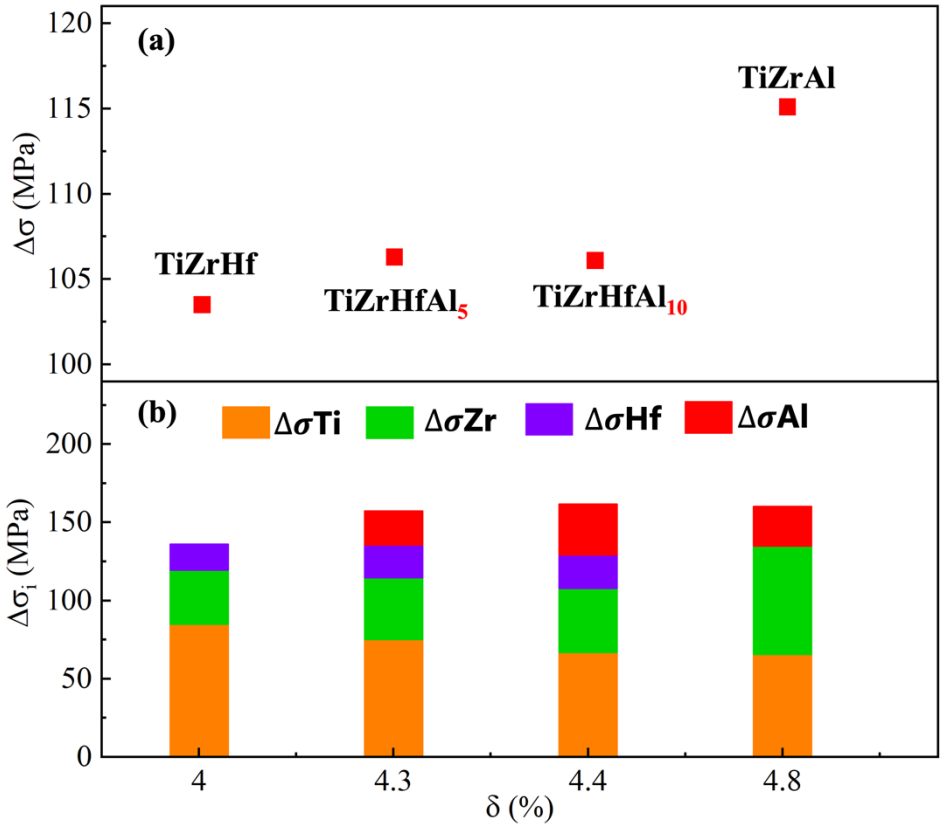

Fig.11 The average atomic radius misfit (δ) values and the solid solution strengthening (SSS, $\Delta\sigma$) values for HCP-MPEAs with equiaxed HCP structure, (a): SSS values for the alloys, and (b): SSS values for each constituent element in the corresponding alloys.

In contrast, the solid solution strengthening in TiZrAl alloy was almost the same as those of TiZrHfAl alloys. This is attributed to the equal ratio of Ti and Zr and the substitution of Hf with Al. This configuration significantly enhances the strengthening effect of Zr ($\Delta\sigma_{Zr}$), while maintaining a comparable strengthening effect for Ti ($\Delta\sigma_{Ti}$) as observed in TiZrHfAl series alloys. The substantial atomic radius mismatch between Zr and both Ti and Al elements is a key factor in this enhancement. Additionally, the primary contribution to the strengthening effect of Zr ($\Delta\sigma_{Zr}$) originates from the Zr-Al interactions.

In addition to the SSS effect, the grain size (Hall–Petch) effect is also a key factor affecting yield strength. For example, although the SSS effect is nearly equal in alloys

$TiZrHfAl_{10}$ and $TiZrHfAl_5$, the smaller grain size of $TiZrHfAl_{10}$ results in a more pronounced Hall-Petch effect, and consequently, higher strength. Conversely, the comparison of the strengths of TiZrHf and TiZrAl alloys suggests that a greater atomic radius misfit can enhance the SSS effect.

5. Conclusions

In the context of limited findings on the mechanical properties, solid solution strengthening, and deformation mechanisms of HCP-MPEAs, this study successfully prepared HCP-MPEAs with a single equiaxed HCP phase through thermomechanical processing and heat treatment. Detailed analyses were conducted to elucidate the solid solution strengthening and deformation mechanisms, with the following key conclusions:

(1) In Ti-containing HCP-MPEAs, through thermomechanical processing (rolling at HCP+BCC phase region) and followed by heat treatment within the HCP single-phase region, we successfully formed single-phase equiaxed HCP structures in TiZrHf, TiZrAl, $TiZrHfAl_5$ and $TiZrHfAl_{10}$ alloys.

(2) The TiZrAl, $TiZrHfAl_5$, and $TiZrHfAl_{10}$ alloys exhibit excellent 0.2% proof strength from room temperature up to 600 °C. Notably, $TiZrHfAl_5$ and $TiZrHfAl_{10}$ alloys demonstrated higher strengths at 600°C compared to the current commercial high temperature alloys such as TIMETAL834 and Ti6242S. Additionally, the 0.2% proof stress tends to increase with increasing mixing entropy (ΔS_{mix}) and the average atomic radius misfit (δ).

(3) Computational simulations indicate that the solid solution strengthening (SSS) effect primarily increases with greater atomic radius misfit (δ), aligning with the observed strength trend of the alloys. The higher atomic radius misfit caused by Al element and electron charge density in the (Ti, Hf, Zr)-Al chemical pairs contribute significantly to this solid solution strengthening effect.

(4) As in conventional HCP alloys, $(10\bar{1}0)$ prismatic slip is the dominant deformation mechanism at 2% plastic deformation.

(5) Larger stress exponent (n) and smaller activation volumes (V^*) than those of conventional alloys suggest that: as described in the Labusch model, deformation is primarily attributed to dislocation motion overcoming small obstacles formed by multiple elements and short-range order (SRO).

Acknowledgments

We express our sincere gratitude to Mr. K. Iida, Mr. M. Kobayashi, and Mr. S. Iwasaki

at NIMS (National Institute for Materials Science) Japan for their assistance in melting and rolling the ingots. We also thank Ms. Y. Nishimiya and Ms. Y. Nakayama at NIMS-ARIM for their support in TEM sample preparation. Additionally, we are grateful to Dr. D. Hamane at the Institute for Solid State Physics (ISSP) of The University of Tokyo for conducting the TEM observations. We also appreciate Prof. Goro Miyamoto, Tohoku University for the useful discussion about slip systems.

Funding sources

This work was supported by Grants-in Aid for Transformative Research Area A, 21H05198 and The Light Metal Educational Foundation (Japan).

Declaration of generative AI in scientific writing

During the preparation of this work, the authors used Grammary and ChatGPT in order to improve the readability and language of this work. After using this tool, the authors reviewed and edited the content as needed and took full responsibility for the publication's content.

Data Availablity

The raw/processed data required to reproduce these findings cannot be shared at this time as the data also forms part of an ongoing study.

Reference

[1] N. Birbilis, S. Choudhary, J.R. Scully, M.L. Taheri, A perspective on corrosion of multi-principal element alloys, Npj Mater Degrad 5 (2021) 14. https://doi.org/10.1038/s41529-021-00163-8.

[2] U.S. Anamu, O.O. Ayodele, E. Olorundaisi, B.J. Babalola, P.I. Odetola, A. Ogunmefun, K. Ukoba, T.-C. Jen, P.A. Olubambi, Fundamental design strategies for advancing the development of high entropy alloys for thermo-mechanical application: A critical review, Journal of Materials Research and Technology 27 (2023) 4833–4860. https://doi.org/10.1016/j.jmrt.2023.11.008.

[3] M.H. Tsai, J.W. Yeh, High-Entropy Alloys: A Critical Review, Mater Res Lett 2 (2014) 107–123. https://doi.org/10.1080/21663831.2014.912690.

[4] W. Li, D. Xie, D. Li, Y. Zhang, Y. Gao, P.K. Liaw, Mechanical behavior of high-entropy alloys, Prog Mater Sci 118 (2021) 100777. https://doi.org/10.1016/j.pmatsci.2021.100777.

[5] Y.L. Zhao, T. Yang, Y.R. Li, L. Fan, B. Han, Z.B. Jiao, D. Chen, C.T. Liu, J.J.

Kai, Superior high-temperature properties and deformation-induced planar faults in a novel L12-strengthened high-entropy alloy, Acta Mater 188 (2020) 517–527. https://doi.org/10.1016/j.actamat.2020.02.028.

[6] K. Zhang, F. He, Z. Yang, D. Cui, J. Li, Z. Yang, J. Wang, Z. Wang, Effect of Re and Ru on the phase stability and coarsening kinetics of L12 phase in a Ni29Co27Fe27Cr3Al7Ti7 high entropy alloy, J Alloys Compd 866 (2021) 158904. https://doi.org/10.1016/j.jallcom.2021.158904.

[7] Y.T. Chen, Y.J. Chang, H. Murakami, S. Gorsse, A.-C. Yeh, Designing high entropy superalloys for elevated temperature application, Scr Mater 187 (2020) 177–182. https://doi.org/10.1016/j.scriptamat.2020.06.002.

[8] E.P. George, W.A. Curtin, C.C. Tasan, High entropy alloys: A focused review of mechanical properties and deformation mechanisms, Acta Mater 188 (2020) 435–474. https://doi.org/10.1016/j.actamat.2019.12.015.

[9] S. Yoshida, T. Ikeuchi, T. Bhattacharjee, Y. Bai, A. Shibata, N. Tsuji, Effect of elemental combination on friction stress and Hall-Petch relationship in face-centered cubic high / medium entropy alloys, Acta Mater 171 (2019) 201–215. https://doi.org/10.1016/j.actamat.2019.04.017.

[10] R. Zhang, S. Zhao, J. Ding, Y. Chong, T. Jia, C. Ophus, M. Asta, R.O. Ritchie, A.M. Minor, Short-range order and its impact on the CrCoNi medium-entropy alloy, Nature 581 (2020) 283–287. https://doi.org/10.1038/s41586-020-2275-z.

[11] S.I. Rao, C. Varvenne, C. Woodward, T.A. Parthasarathy, D. Miracle, O.N. Senkov, W.A. Curtin, Atomistic simulations of dislocations in a model BCC multicomponent concentrated solid solution alloy, Acta Mater 125 (2017) 311–320. https://doi.org/10.1016/j.actamat.2016.12.011.

[12] F. Maresca, W.A. Curtin, Theory of screw dislocation strengthening in random BCC alloys from dilute to “High-Entropy” alloys, Acta Mater 182 (2020) 144–162. https://doi.org/10.1016/j.actamat.2019.10.007.

[13] A. Takeuchi, K. Amiya, T. Wada, K. Yubuta, W. Shang, High-entropy alloys with a hexagonal close-packed structure designed by equi-atomic alloy strategy and binary phase diagrams, JOM 66 (2014) 1984–1992. https://doi.org/10.1007/s11837-014-1085-x.

[14] M. Feuerbacher, M. Heidelmann, C. Thomas, Hexagonal high-entropy alloys, Mater. Res. Lett. 3 (2015) 1–6. http://dx.doi.org/10.1080/21663831.2014.951493.

[15] Y. J. Zhao, J. W. Qiao, S. G. Ma, M. C. Gao, H. J. Yang, M. W. Chen, Y. Zhang, A hexagonal close-packed high-entropy alloy: The effect of entropy, Mater. Des. 96 (2016) 10-15. https://doi.org/10.1016/j.matdes.2016.01.149

[16] J. W. Qiao, M. L. Bao, Y. J. Zhao, h. J. Yang, Y. C. Wu, Y. Zhang, J. A. Hawk, M. C. Gao, Rare-earth high entropy alloys with hexagonal close-packed structure, J Appl Phys, 124, 19 (2018) 195101, https://doi.org/10.1063/1.5051514.

[17] R. Soler, A. Evirgen, M. Yao, C. Kirchlechner, F. Stein, M. Feuerbacher, D. Raabe, G. Dehm, Microstructural and mechanical characterization of an equiatomic YGdTbDyHo high entropy alloy with hexagonal close-packed structure, Acta materialia, 156, (2018) 86-96. https://doi.org/10.1016/j.actamat.2018.06.01

[18] Z. Wang, M. L. Bao, X. J. Wang, P. K. Liaw, R. P. Guo, J. W. Qiao, Deformation mechanisms in hexagonal close-packed high-entropy alloys, J. Appl. Phys., 129, 17 (2021) 175104. https://doi.org/10.1063/5.0045414

[19] Z. Wang, X. W. Yang, Q. Zhang, J. W. Qiao, Nanoindentation creep behavior of hexagonal close-packed high-entropy alloys, Met. Mater. Int., 30 (2024) 2433-2439. https://doi.org/10.1007/s12540-024-01655-3.

[20] Y. Yuan, Y. Wu, Z. Tong, H. Zhang, H. Wang, X. J, Liu, L, Ma, H. L. Suo, Z. P. Lu, Rare-earth high-entropy alloys with giant magnetocaloric effect, Acta Mtaer. 125 (2017) 481-489. https://doi.org/10.1016/j.actamat.2016.12.021

[21] S. Vrtnik, J. Lužnik, P. Koželj, A. Jelen, J. Luzar, Z. Jagličić, A. Meden, M. Feuerbacher, J. Dolinšek Disordered ferromagnetic state in the Ce-Gd-Tb-Dy-Ho hexagonal high-entropy alloy, J Alloys Compd, 742, (2018) 877–886 https://doi.org/10.1016/j.jallcom.2018.01.331.

[22] M.C. Gao, B. Zhang, S. M. Guo, J. W. Qiao, J. A. Hawk, High-Entropy Alloys in Hexagonal Close-Packed Structure, Metall Mater Trans A, 47, (2016) 3322–3332. https://doi.org/10.1007/s11661-015-3091-1.

[23] A. Takeuchi, T. Wada, and H. Kato, High-entropy alloys with hexagonal close-packed structure in $Ir_{26}Mo_{20}Rh_{22.5}Ru_{20}W_{11.5}$ and $Ir_{25.5}Mo_{20}Rh_{20}Ru_{25}W_{9.5}$ alloys designed by sandwich strategy for the valence electron concentration of constituent elements in the periodic chart, Mater. Trans. 60 (2019) 1666–1673. https://doi.org/10.2320/matertrans.M2019037.

[24] A. Takeuchi, T. Wada, and H. Kato, Solid solutions with bcc, hcp, and fcc structures formed in a composition line in multicomponent Ir-Rh-Ru-W-Mo system, Mater. Trans. 60 (2019) 2267–2276. https://doi.org/10.2320/matertrans.MT-M2019212.

[25] S. Matsunaga, O. Shimizu, S. Liang, Y-N. Shen, Y. Yamabe-Mitarai, The effect of constituent phase on microstructure and high temperature deformation mechanisms of IrRhRuWMo complex concentrated alloys, Mater. Sci. Eng. A, 913 (2024) 147018. https://doi.org/10.1016/j.msea.2024.147018

[26] K. V. Yusenko, S. Riva, P. A. Carvalho, M. V. Yusenko, S. Arnaboldi, A. S. Sukhikh,

M. Hanfland, S. A. Gromilov, First hexagonal close packed high-entropy alloy with outstanding stability under extreme conditions and electrocatalytic activity for methanol oxidation, Scripta Materialia, 138 (2017) 22-27. https://doi.org/10.1016/j.scriptamat.2017.05.022. (2017).

[27] T. H. Hu, C. Y. Wu, Z. Y. He, Y. Chen, L. C. Hsu, C. W. Pao, j. T. Lin, C. W. Chang, S. C. Lin, R. Osmundsen, L. Casalena, K. H. Lin, S. Zhou, T. H. Yang, Unconventional Hexagonal Close-Packed High-Entropy Alloy Surfaces Synergistically Accelerate Alkaline Hydrogen Evolution, Advanced Science, (2024) 2409023. https://doi.org/10.1002/advs.202409023.

[28] K. Motla, S. Jangid, P. K. Meena, R. K. Kushwaha, R. P. Singh, Superconducting properties of new hexagonal and noncentrosymmetric cubic high entropy alloys, Superconductor Science and Technology, 36, 11 (2023) 115024. https://doi.org/10.1088/1361-6668/acfac5

[29] X. Xu, W. Yang, H. Song, J. Wang, L. Yu, Z. Ren, B. Liu, Structural sequence and superconductivity in high-entropy Mo-W-Re-Ru-Pd alloys, Scripta Materialia, 243 (2024), 115986. https://doi.org/10.1016/j.scriptamat.2024.115986.

[30] T. Huang, H. Jiang, Y. Lu, T. Wang, T. Li, Effect of Sc and Y addition on the microstructure and properties of HCP-structured high-entropy alloys, Appl. Phys. A 125 (2019) 180. https://doi.org/10.1007/s00339-019-2484-1.

[31] S. Wang, D. Wu, H. She, M. Wu, D. Shu, A. Dong, H. Lai, B. Sun, Design of high-ductile medium entropy alloys for dental implants, Mater. Sci. Eng. C 113 (2020) 110959. https://doi.org/10.1016/j.msec.2020.110959.

[32] Y. Yamabe-Mitarai, K. Yanao, Y. Toda, I. Ohnuma, T. Matsunaga, Phase stability of Ti-containing high-entropy alloys with a bcc or hcp structure, J. Alloys Compds, 911 (2022) 164849. https://doi.org/10.1016/j.jallcom.2022.164849.

[33] S.J. Liang, S. Matsunaga, Y. Toda, Y. Yamabe-Mitarai, Microstructure evolution by thermomechanical processing and high-temperature mechanical properties of HCP-high entropy alloys (HEAs), Mater. Sci. and Eng. A, 918 (2024) 147414. https://doi.org/10.1016/j.msea.2024.147414.

[34] J. Kuang, D. Zhang, Y. Zhang, X. Du, Q. Huo, W. Wen, F. Tian, G. Liu, J. Zhang, J. Sun, Achieving excellent strength-toughness combination in hexagonal closed-packed multi-principle element alloys via 〈c + a〉 slip promotion, Scr. Mater. 242 (2024) 115903. https://doi.org/10.1016/j.scriptamat.2023.115903.

[35] G. M. Muralikrishna, S. Sen, S. K.Ayyappan, S. Sankaran, K. Guruvidyathri, J. Schell, Ł. Rogal, X. Zhang, J. Mayer, B. Grabowski, G. Wilde, S. V. Divinski,

Microstructure stability and self-diffusion in the equiatomic HfScTiZr HCP multi-principal element alloy, J. Alloys Compds, 976 (2024) 173196. https://doi.org/10.1016/j.jallcom.2023.173196

[36] Ł. Rogal, F. Czerwinski, P.T. Jochym, L. Litynska-Dobrzynska, Microstructure and mechanical properties of the novel $Hf_{25}Sc_{25}Ti_{25}Zr_{25}$ equiatomic alloy with hexagonal solid solutions, Mater. Des. 92 (2016) 8–17. https://doi.org/10.1016/j.matdes.2015.11.104.

[37] S. Uporov, S. K. h. Estemirova, V. A. Bykov, D. A. Zamyatin, R. E. Ryltsev, A single-phase ScTiZrHf high-entropy alloy with thermally stable hexagonal close-packed structure, Intermetallics 122 (2020) 106802. https://doi.org/10.1016/j.intermet.2020.106802.

[38] G. M. Muralikrishna, S. Sen, S. K. Ayyappan, S. Sankaran, K. Guruvidyathri, J. Schell, Ł. Rogal, X. Zhang, J. Mayer, B. Grabowski, G. Wilde, S. V. Divinski, Microstructure stability and self-diffusion in the equiatomic HfScTiZr HCP multi-principal element alloy, J. Alloys Compds, 976 (2024) 173196. https://doi.org/10.1016/j.jallcom.2023.173196

[39] Ł. Rogal, J. Morgiel, Z. Świątek, F. Czerwiński, Microstructure and mechanical properties of the new $Nb_{25}Sc_{25}Ti_{25}Zr_{25}$ eutectic high entropy alloy, Mater. Sci. Eng. A 651 (2016) 590–597. https://doi.org/10.1016/j.msea.2015.10.071.

[40] Ł. Rogal, P. Bobrowski, F. Körmann, S. Divinski, F. Stein, B. Grabowski, Computationally-driven engineering of sublattice ordering in a hexagonal AlHfScTiZr high entropy alloy, Scientific Reports 7 (2017) 2209. https://doi.org/10.1038/s41598-017-02385-w.

[41] X. T. Chen, L. Shao, T. W. Fan, J. M. Duan, B. Y. Tang, Investigation of aluminum concentration on stacking fault energies of hexagonal close-packed high-entropy alloys $Hf_{0.25}Ti_{0.25}Zr_{0.25}Sc_{0.25-x}Al_x$ (x< 15%), J. Alloys Compds, 887 (2021) 161412. https://doi.org/10.1016/j.jallcom.2021.161412.

[42] S. Sen, X. Zhang, L. Rogal, G. Wilde, B. Grabowski, S. V. Divinski, Does Zn mimic diffusion of Al in the HCP Al-Sc-Hf-Ti-Zr high entropy alloys?, Scripta Materialia, 229 (2023) 115376. https://doi.org/10.1016/j.scriptamat.2023.115376.

[43] M. Vaidya, S. Sen, X. Zhang, L. Frommeyer, Ł. Rogal, S. Sankaran, B. Grabowski, G. Wide, S. V. Diviniski, Phenomenon of ultra-fast tracer diffusion of Co in HCP high entropy alloys, Acta Mater., 196 (2020) 220-230. https://doi.org/10.1016/j.actamat.2020.06.025

[44] G-Y. Gan, L. Ma, D-M. Luo, S. Jiang, B-Y. Tang, Influence of Al substitution for Sc on thermodynamic properties of HCP high entropy alloy

$Hf_{0.25}Ti_{0.25}Zr_{0.25}Sc_{0.25-x}Al_x$ from first-principles investigation, Phys. B 593 (2020) 412272. https://doi.org/10.1016/j.physb.2020.412272.

[45] Ł. Rogal, Y. Ikeda, M. Lai, F. Körmann, A. Kalinowska, B. Grabowski, Design of a dual-phase hcp-bcc high entropy alloy strengthened by ω nanoprecipitates in the Sc-Ti-Zr-Hf-Re system, Mater. Des. 192 (2020) 108716. https://doi.org/10.1016/j.matdes.2020.108716.

[46] T. Nagase, M. Todai, T. Nakano, Development of Ti-Zr-Hf-Y-La high-entropy alloys with dual hexagonal-close-packed structure, Scr. Mater. 186 (2020) 242–246. https://doi.org/10.1016/j.scriptamat.2020.05.033.

[47] A. Takeuchi, K Amiya, T. Wada, and H. Yubuta, Dual HCP structures formed in senary ScYLaTiZrHf multi-principal-element alloy, Intermetallics 69 (2016) 103–109. http://dx.doi.org/10.1016/j.intermet.2015.10.022.

[48] Ł. Rogal, U.D. Wdowik, M. Szczerba, N. Yurchenko, T. Czeppe, P. Bobrowski, Deformation induced twinning in hcp/bcc $Al_{10}Hf_{25}Nb_5Sc_{10}Ti_{25}Zr_{25}$ high entropy alloy – microstructure and mechanical properties, Mater. Sci. Eng. A 802 (2021) 140449. https://doi.org/10.1016/j.msea.2020.140449.

[49] P. Giannozzi, S. Baroni, N. Bonini, M. Calandra, R. Car, C. Cavazzoni, D. Ceresoli, G.L. Chiarotti, M. Cococcioni, I. Dabo, A. Dal Corso, S. de Gironcoli, S. Fabris, G. Fratesi, R. Gebauer, U. Gerstmann, C. Gougoussis, A. Kokalj, M. Lazzeri, L. Martin-Samos, N. Marzari, F. Mauri, R. Mazzarello, S. Paolini, A. Pasquarello, L. Paulatto, C. Sbraccia, S. Scandolo, G. Sclauzero, A.P. Seitsonen, A. Smogunov, P. Umari, R.M. Wentzcovitch, QUANTUM ESPRESSO: a modular and open-source software project for quantum simulations of materials, Journal of Physics: Condensed Matter 21 (2009) 395502. https://doi.org/10.1088/0953-8984/21/39/395502.

[50] P.E. Blöchl, Projector augmented-wave method, Phys Rev B 50 (1994) 17953–17979. https://doi.org/10.1103/PhysRevB.50.17953.

[51] J.P. Perdew, K. Burke, M. Ernzerhof, Generalized Gradient Approximation Made Simple [Phys. Rev. Lett. 77, 3865 (1996)], Phys Rev Lett 78 (1997) 1396–1396. https://doi.org/10.1103/PhysRevLett.78.1396.

[52] A. Zunger, S.-H. Wei, L.G. Ferreira, J.E. Bernard, Special quasirandom structures, Phys Rev Lett 65 (1990) 353–356. https://doi.org/10.1103/PhysRevLett.65.353.

[53] A. van de Walle, P. Tiwary, M. de Jong, D.L. Olmsted, M. Asta, A. Dick, D. Shin, Y. Wang, L.-Q. Chen, Z.-K. Liu, Efficient stochastic generation of special quasirandom structures, Calphad 42 (2013) 13–18.

https://doi.org/10.1016/j.calphad.2013.06.006.
[54] G. Lütjering, Influence of processing on microstructure and mechanical properties of (α+β) titanium alloys, Materials Science and Engineering: A 243 (1998) 32–45. https://doi.org/10.1016/S0921-5093(97)00778-8.
[55] K. Shimagami, T. Ito, Y. Toda, A. Yumoto, Y. Yamabe-Mitarai, Effects of Zr and Si addition on high-temperature mechanical properties and microstructure in Ti-10Al-2Nb-based alloys, Materials Science and Engineering A 756 (2019) 46–53. https://doi.org/10.1016/j.msea.2019.04.031.
[56] Z. Tobolová, J. Čadek, An interpretation of steady state creep, Philosophical Magazine 26 (1972) 1419–1428. https://doi.org/10.1080/14786437208220352.
[57] H. Mishra, D. Satyanarayana, T. Nandy, P. Sagar, Effect of trace impurities on the creep behavior of a near α titanium alloy, Scr Mater 59 (2008) 591–594. https://doi.org/10.1016/j.scriptamat.2008.05.009.
[58] Z.Y. Ma, R.S. Mishra, S.C. Tjong, High-temperature creep behavior of TiC particulate reinforced Ti–6Al–4V alloy composite, Acta Mater 50 (2002) 4293–4302. https://doi.org/10.1016/S1359-6454(02)00261-6.
[59] J.L.M. D. Caillard, Thermally activated mechanisms in crystal plasticity, Elsevier, Amsterdam, 2003.
[60] R.J. Asaro, S. Suresh, Mechanistic models for the activation volume and rate sensitivity in metals with nanocrystalline grains and nano-scale twins, Acta Mater 53 (2005) 3369–3382. https://doi.org/10.1016/j.actamat.2005.03.047.
[61] S. Zhang, W. Zeng, Q. Zhao, L. Ge, M. Zhang, In situ SEM study of tensile deformation of a near-β titanium alloy, Materials Science and Engineering: A 708 (2017) 574–581. https://doi.org/10.1016/j.msea.2017.10.028.
[62] Y. Li, P. Gao, J. Yu, S. Jin, S. Chen, M. Zhan, Mesoscale deformation mechanisms in relation with slip and grain boundary sliding in TA15 titanium alloy during tensile deformation, J Mater Sci Technol 98 (2022) 72–86. https://doi.org/10.1016/j.jmst.2021.05.008.
[63] M.H. Yoo, Slip, twinning, and fracture in hexagonal close-packed metals, Metallurgical Transactions A 12 (1981) 409–418. https://doi.org/10.1007/BF02648537.
[64] J.M. Duan, L. Shao, T.W. Fan, X.T. Chen, B.-Y. Tang, Intrinsic mechanical properties of hexagonal multiple principal element alloy TiZrHf: An ab initio prediction, Int J Refract Metals Hard Mater 100 (2021) 105626. https://doi.org/10.1016/j.ijrmhm.2021.105626.
[65] X. Liu, Q. Zhang, X. Yang, X. He, S. Kang, F. Gao, Deformation, Strain Rate

Sensitivity and Activation Volume of Ultrafine-grained Commercially Pure Ti, Rare Metal Materials and Engineering 49 , 6(2020) 1867–1872.

[66] B.R. Anne, M. Tanaka, T. Morikawa, Temperature Dependence of Activation Enthalpy for Yielding in Bimodal Ti–6Al–4V, Mater Trans 60 (2019) 1828–1832. https://doi.org/10.2320/matertrans.ME201902.

[67] H. Somekawa, C.A. Schuh, Effect of solid solution elements on nanoindentation hardness, rate dependence, and incipient plasticity in fine grained magnesium alloys, Acta Mater 59 (2011) 7554–7563. https://doi.org/10.1016/j.actamat.2011.08.047.

[68] S.I. Hong, J. Moon, S.K. Hong, H.S. Kim, Thermally activated deformation and the rate controlling mechanism in CoCrFeMnNi high entropy alloy, Materials Science and Engineering: A 682 (2017) 569–576. https://doi.org/10.1016/j.msea.2016.11.078.

[69] Y. Xiao, R. Kozak, M.J.R. Haché, W. Steurer, R. Spolenak, J.M. Wheeler, Y. Zou, Micro-compression studies of face-centered cubic and body-centered cubic high-entropy alloys: Size-dependent strength, strain rate sensitivity, and activation volumes, Materials Science and Engineering: A 790 (2020) 139429. https://doi.org/10.1016/j.msea.2020.139429.

[70] R. Labusch, A Statistical Theory of Solid Solution Hardening, Physica Status Solidi (b) 41 (1970) 659–669. https://doi.org/10.1002/pssb.19700410221.

[71] Z. Wu, Y. Gao, H. Bei, Thermal activation mechanisms and Labusch-type strengthening analysis for a family of high-entropy and equiatomic solid-solution alloys, Acta Mater 120 (2016) 108–119. https://doi.org/10.1016/j.actamat.2016.08.047.

[72] S. Yoshida, T. Ikeuchi, T. Bhattacharjee, Y. Bai, A. Shibata, N. Tsuji, Effect of elemental combination on friction stress and Hall-Petch relationship in face-centered cubic high / medium entropy alloys, Acta Mater 171 (2019) 201–215. https://doi.org/10.1016/j.actamat.2019.04.017.

[73] Z. Zheng, D.S. Balint, F.P.E. Dunne, Rate sensitivity in discrete dislocation plasticity in hexagonal close-packed crystals, Acta Mater 107 (2016) 17–26. https://doi.org/10.1016/j.actamat.2016.01.035.

[74] D. Caillard, M. Gaumé, F. Onimus, Glide and cross-slip of a-dislocations in Zr and Ti, Acta Mater 155 (2018) 23–34. https://doi.org/10.1016/j.actamat.2018.05.038.

[75] I. Toda-Caraballo, P.E.J. Rivera-Díaz-del-Castillo, Modelling solid solution hardening in high entropy alloys, Acta Mater 85 (2015) 14–23.

https://doi.org/10.1016/j.actamat.2014.11.014.
[76] J.W. Qiao, M.L. Bao, Y.J. Zhao, H.J. Yang, Y.C. Wu, Y. Zhang, J.A. Hawk, M.C. Gao, Rare-earth high entropy alloys with hexagonal close-packed structure, J Appl Phys 124 (2018). https://doi.org/10.1063/1.5051514.
[77] P. Lukáč, Solid solution hardening in MgCd single crystals, Physica Status Solidi (a) 131 (1992) 377–390. https://doi.org/10.1002/pssa.2211310212.
[78] R.L. Fleischer, Substitutional solution hardening, Acta Metallurgica 11 (1963) 203–209. https://doi.org/10.1016/0001-6160(63)90213-X.
[79] L.A. Gypen, A. Deruyttere, Multi-component solid solution hardening, J Mater Sci 12 (1977) 1028–1033. https://doi.org/10.1007/BF00540987.
[80] O.N. Senkov, J.M. Scott, S.V. Senkova, D.B. Miracle, C.F. Woodward, Microstructure and room temperature properties of a high-entropy TaNbHfZrTi alloy, J Alloys Compd 509 (2011) 6043–6048. https://doi.org/10.1016/j.jallcom.2011.02.171.
[81] Y.F. Ye, Q. Wang, J. Lu, C.T. Liu, Y. Yang, High-entropy alloy: challenges and prospects, Materials Today 19 (2016) 349–362. https://doi.org/10.1016/j.mattod.2015.11.026.